

---

# CD-RCM: Generalizable Continuous-Depth Novel View Synthesis for Reflectance Confocal Microscopy

---

Tooba Imtiaz<sup>1</sup>, Milind Rajadhyaksha<sup>2</sup>, Kivanc Kose<sup>2,\*</sup>, Jennifer Dy<sup>1,\*</sup>

<sup>1</sup>Northeastern University, <sup>2</sup>Memorial Sloan Kettering Cancer Center  
 {imtiaz.t, j.dy}@northeastern.edu, {rajadhym, kosek}@mskcc.org

\* denotes equal contribution

## Abstract

Reflectance confocal microscopy (RCM) provides noninvasive, cellular-resolution “optical biopsies” of human skin *in vivo* by acquiring en-face images at successive depths, forming a sparse  $z$ -stack. Due to optical limitations, these stacks are anisotropic 3D volumes with lateral resolution ( $0.5\mu\text{m}$ )  $\sim 6$  times higher compared to axial resolution, which is defined by the optical sectioning ( $3\mu\text{m}$ ), limiting the interpretation of tissue. Our goal is to provide continuous-depth visualization by interpolating intermediate sections and making the 3D volume isotropic. Such a representation permits arbitrary-direction sectioning, including histopathology-like cross-sectional examination, without requiring per-patient optimization. To that end, we introduce the first RCM-specific novel-view synthesis (NVS) approach, CD-RCM, a feedforward model that predicts realistic, unseen depths from sparsely sampled RCM stacks. Classical neural rendering methods focus on reconstruction from surface-level multi-view observations. In contrast to surface-level camera views, RCM can acquire optically sectioned en-face images of tissue beyond the surface up to  $200\mu\text{m}$ . However, during visualization of the RCM stacks, observations of the shallower sections (towards the surface) obscure the deeper ones. This unique axial imaging geometry and layer-dependent anatomical organization motivated our development of a tailored architectural and training framework that explicitly accounts for RCM’s depth-resolved, occlusive imaging physics. Experiments demonstrate that CD-RCM achieves high-fidelity novel-view synthesis with sub-second inference time.

## 1 Introduction

Early detection and precise staging of skin disease rely on observing microstructural changes across depth, often beginning at anatomically meaningful boundaries such as the dermal–epidermal junction (DEJ). Optical sectioning microscopy techniques like Reflectance Confocal Microscopy (RCM) [Gonzalez et al., 2008] enable noninvasive *in vivo* imaging of skin with near-histologic resolution and are widely used for diagnosing tumors, inflammatory conditions, and guiding surgical margin assessment [Edwards et al., 2017, Huzaira et al., 2001, Wojarska et al., 2025, Richarz et al., 2022].

Clinicians acquire RCM data as  $z$ -stacks — sequences of en-face optical sections sampled at discrete depths. Although lateral resolution is high ( $\sim 0.5\mu\text{m}$ ), axial resolution is governed by optical sectioning ( $\sim 3\mu\text{m}$ ), resulting in strongly anisotropic volumes that limit depth-wise interpretation, particularly near diagnostically critical transitions such as the DEJ. Prior studies note the tradeoff between slice spacing and acquisition time, and the sensitivity of downstream algorithms to sampling density [Bozkurt et al., 2017, Ghanta et al., 2016]. Conventional interpolation methods (*e.g.*, spline-based) lack anatomical priors and fail to preserve depth-dependent skin morphology.

In this work, we introduce *Continuous-Depth Novel-View Synthesis for RCM* (CD-RCM), a feed-forward model for continuous-depth novel-view synthesis from sparse RCM stacks. Our approach leverages the structured axial acquisition process of optical sectioning microscopy and models depth variation as a queryable dimension. Unlike prior methods, CD-RCM predicts anatomically consistent intermediate slices in a single forward pass, without per-stack optimization, and generalizes across patients and imaging sites. Importantly, CD-RCM does not increase intrinsic optical resolution; it enables computational depth densification within the same acquisition constraints under which it is trained, building on recent advances in transformer-based view synthesis [Zhang et al., 2024, Jin et al., 2025, Hong et al., 2024, Imtiaz et al., 2025].

To preserve fine cellular structure, we further propose a *skin-specific perceptual loss*, based on a domain-adapted feature extractor trained on RCM data. This enables the model to capture micro-textural patterns that are not well represented by perceptual losses trained on natural images.

In summary, we make the following contributions:

1. We introduce the first formulation of arbitrary-depth novel-view synthesis for RCM, explicitly addressing the anisotropic and see-through nature of RCM stacks.
2. We develop CD-RCM, a feedforward, depth-queryable model that incorporates the axial imaging physics of RCM and generalizes across skin sites without per-stack optimization.
3. Our experiments demonstrate that CD-RCM achieves high-fidelity novel-depth synthesis in a single inference pass, outperforming conventional interpolation baselines.

## 2 Related Work

Our work draws on two areas of prior research: algorithmic analysis of RCM stacks, and neural methods for 3D reconstruction and novel-view synthesis. We review each below, highlighting how existing methods address related problems but leave a gap at their intersection — namely, feedforward synthesis of arbitrary intermediate depths from sparsely sampled confocal stacks.

### 2.1 RCM stacks and downstream analysis

RCM enables non-invasive, *in vivo* optical sectioning of skin with near-cellular lateral resolution. Unlike conventional histopathology, which provides vertically sectioned, stained tissue spanning multiple layers, RCM produces grayscale *en face* images based on intrinsic reflectance contrast. The *en face* geometry and anisotropic resolution make interpretation challenging, as clinicians must mentally reconstruct cross-sectional structure from sparsely sampled depth stacks.

Prior computational work has focused on algorithmic analysis of discretely acquired stacks — including DEJ localization [Kose et al., 2020, Ghanta et al., 2016], strata delineation, and layer thickness estimation [Bozkurt et al., 2017, 2021] — treating stacks as fixed collections of optical sections rather than modifying or densifying the underlying volume.

From a visualization standpoint, RCM’s anisotropic resolution yields inadequate reconstructions from any angle other than *en face*. Perpendicular sections analogous to histopathology can be constructed from stacks but suffer from sparse axial sampling; naïve interpolation introduces blocking artifacts and unrealistic structures. Dense 3D visualization [Song et al., 2024] could enhance structural understanding of tissue organization, but alternative volumetric modalities such as light-sheet microscopy [Liu et al., 2023] and LC-OCT [Latriglia et al., 2023] are either impractical for routine *in vivo* imaging or offer lower lateral resolution than RCM.

Crucially, each RCM optical section integrates signal from adjacent depths due to the finite axial point-spread function, yet this overlapping information has not been leveraged for dense axial reconstruction. We formulate continuous-depth reconstruction as a feedforward novel-view synthesis problem that exploits this property and the structured axial acquisition geometry to densify sparse stacks without needing per-stack optimization.

### 2.2 Neural rendering, 3D reconstruction and view synthesis

3D reconstruction and novel-view synthesis have progressed from implicit representations [Mescheder et al., 2019, Chibane et al., 2020] to NeRF [Mildenhall et al., 2020] and 3D Gaussian Splatting

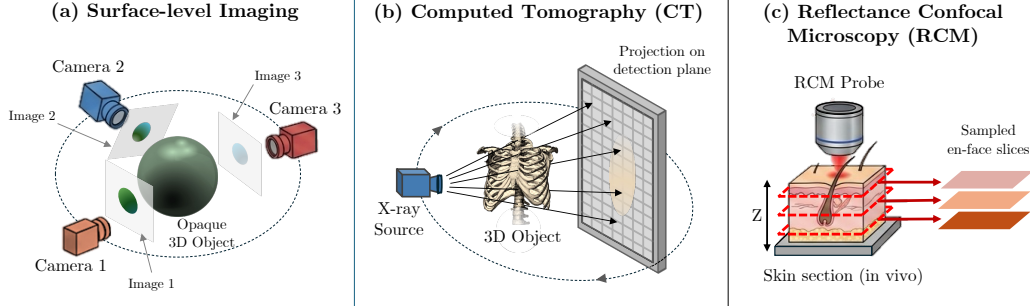


Figure 1: **Comparison of imaging paradigms.** (a) Surface-level imaging reconstructs opaque objects from multiple posed viewpoints with geometric parallax. (b) CT acquires transmission projections from multiple angles and reconstructs 3D structure from X-ray attenuation. (c) RCM performs axial optical sectioning, capturing discrete en-face slices of internal tissue at successive depths.

[Kerbl et al., 2023], enabling increasingly high-fidelity reconstruction with reduced optimization time. However, two limitations persist. Most methods require per-scene optimization, and while recent generalizable frameworks [Charatan et al., 2024, Zhang et al., 2024, Jin et al., 2025, Imtiaz et al., 2025] enable feedforward inference, they are primarily designed for surface-level reconstruction of opaque objects under known camera poses (Figure 1a), offering limited support for internal geometry.

Tomographic reconstruction offers a parallel perspective, as recovering 3D structure from sparse measurements is an ill-posed inverse problem (Figure 1b). Recent radiative Gaussian splatting approaches [Cai et al., 2024, Zha et al., 2024, Li et al., 2025] tailor rendering operators to X-ray physics for sparse-view CT, but like surface-based NVS methods, they require per-case optimization and do not generalize across subjects or hardware settings without retraining.

As illustrated in Figure 1, RCM occupies a distinct regime that differs fundamentally from both surface-level and CT imaging modalities. Unlike standard NVS, RCM captures internal tissue via axial optical sectioning with minimal viewpoint variation; unlike CT, its contrast is governed by depth-dependent tissue optics rather than geometric parallax. These properties motivate a specialized, generalizable approach for depth-conditioned synthesis of en face sections from sparse axial stacks.

### 3 Method

CD-RCM builds upon transformer-based novel-view synthesis architectures [Charatan et al., 2024, Zhang et al., 2024, Jin et al., 2025], adapting them to model internal skin structures captured by reflectance confocal microscopy. We describe our components below and highlight key differences from conventional surface-level NVS frameworks.

#### 3.1 Overview

An RCM *stack* consists of  $N$  en-face grayscale images  $\mathbf{I}_i \in \mathbb{R}^{H \times W}$ ,  $i = 1 \dots N$ , each comprising a  $3 \mu\text{m}$  thick optical section of tissue. By moving the focusing depth through the tissue, the microscope translates the focal plane along the axial ( $z$ ) direction at  $>1.5 \mu\text{m}$  steps with negligible lateral ( $x, y$ ) motion, imaging up to  $150\text{--}200 \mu\text{m}$  deep. Stacks typically contain  $50\text{--}65$  slices.

RCM does not operate as a conventional camera-based imaging system. Instead, it raster-scans a focused beam using galvanometric mirrors and collects back-scattered light through a confocal pinhole, which enforces optical sectioning and provides depth selectivity. Since each slice corresponds to a fixed lateral field of view at a known axial position, we approximate the imaging process as a virtual pinhole camera undergoing pure  $z$ -axis translation (Section 3.2). This abstraction enables us to leverage Plücker ray embeddings and transformer architectures designed for multi-view geometry.

Given sparse inputs  $\mathbf{I}_i$ , CD-RCM synthesizes target slices  $\mathbf{I}_t$  at arbitrary unseen depths (Figure 2) within the range of the collected stack. As illustrated in Figure 2, we map input slices and their corresponding Plücker embeddings into a unified token space, process them using a decoder-only transformer, and decode only the updated target tokens to generate  $\hat{\mathbf{I}}_t$ . We train the model using a

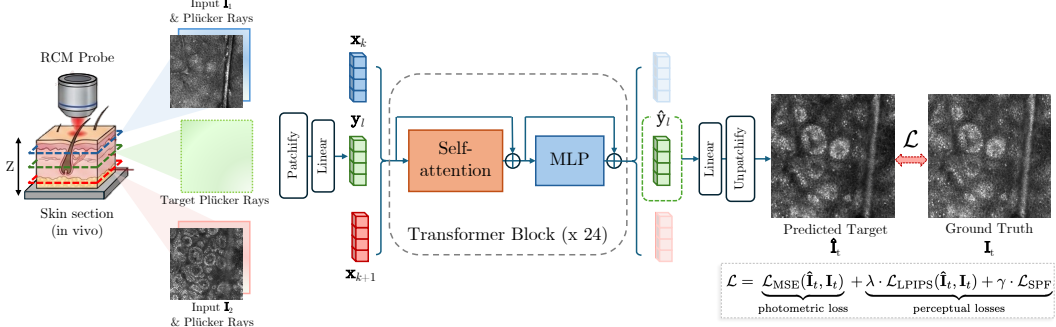


Figure 2: **Overview of CD-RCM.** Sparse input RCM slices and their Plücker ray embeddings are mapped to a unified token space and processed by a decoder-only transformer. Target ray tokens condition the synthesis; updated target tokens are decoded to produce  $\hat{I}_t$ . Training uses a weighted combination of photometric, LPIPS, and skin-specific perceptual feature loss  $\mathcal{L}_{\text{SPF}}$ .

combination of photometric reconstruction loss and perceptual supervision, including our proposed skin-specific perceptual feature loss.

Below, we describe the virtual camera parameters (Section 3.2), skin-specific perceptual feature extractor (Section 3.4), CD-RCM architecture (Section 3.3), and overall training objective (Section 3.5).

### 3.2 Virtual Camera Parameters

RCM forms images via a scanning laser and confocal pinhole that optically section tissue at controlled focal depths. Although no physical camera parameters are available, the acquisition process provides strong geometric priors, *i.e.*, consecutive slices share the same lateral field of view and differ primarily in axial position. Note that, unlike surface-level datasets, where pose estimation requires feature matching across viewpoints, RCM stacks exhibit near-perfect lateral alignment and systematic axial translation. Inter-slice correspondence arises from imaging different axial sections of the same underlying three-dimensional tissue structures (e.g., cells, vessels, and collagen), rather than from observing a static object under varying viewpoints. Consequently, the depth variation reflects progressive optical sectioning rather than geometric parallax. We exploit this by modeling acquisition as a virtual pinhole camera with fixed orientation translating along  $z$ .

Let slice index  $i \in \{1, \dots, N\}$  denote the depth position within a stack. We approximate the camera motion as a pure translation, *i.e.*,  $\mathbf{c}_i = [0, 0, z_i]^T$ ,  $z_i = i \cdot \Delta_z$ . Here  $\Delta_z$  is a constant axial step size. In practice,  $\Delta_z$  corresponds to the physical spacing between optical sections (approximately  $3\mu\text{m}$ ), mapped to normalized model coordinates.

Assuming fixed camera orientation, the world-to-camera transform is

$$\mathbf{T}_{\text{w2c}}^{(i)} = \begin{bmatrix} \mathbf{I}_3 & \mathbf{c}_i \\ \mathbf{0}^\top & 1 \end{bmatrix} \quad (1)$$

where  $\mathbf{I}_3$  denotes identity rotation. Neural rendering formulations typically adopt the camera-to-world convention. Since the transform is purely translational, its inverse admits a closed-form expression:

$$\mathbf{T}_{\text{c2w}}^{(i)} = \begin{bmatrix} \mathbf{I}_3 & -\mathbf{c}_i \\ \mathbf{0}^\top & 1 \end{bmatrix} \quad (2)$$

This matrix defines the camera pose associated with slice  $I_i$ .

**Stack Canonicalization.** Although poses are synthetically constructed, per-stack normalization improves numerical stability and learning consistency across stacks. Given a set of translations  $\{\mathbf{c}_i\}$ , we compute the mean camera center  $\bar{\mathbf{c}} = \frac{1}{N} \sum_{i=1}^N \mathbf{c}_i$  and the maximum absolute translation  $\mathbf{c}_\infty = \max_{i \in \{1, \dots, N\}} \|\mathbf{c}_i\|_\infty$  to standardize all poses via  $\mathbf{c}_i \leftarrow (\mathbf{c}_i - \bar{\mathbf{c}})/\mathbf{c}_\infty$ . This embeds each stack within a shared normalized coordinate system while preserving relative depth relations.

**Camera Intrinsic Parameters** Camera intrinsics  $K$  are similarly approximated using a fixed pinhole model:

$$\mathbf{K} = \begin{bmatrix} f_x & 0 & u_0 \\ 0 & f_y & v_0 \\ 0 & 0 & 1 \end{bmatrix} \quad (3)$$

where focal lengths are set proportional to image resolution, *i.e.*,  $f_x = f_y = \alpha H$ , with  $\alpha$  a constant scaling factor, and  $u_0 = v_0 = \frac{H}{2}$ . Altogether, this approximation provides a stable geometric reference without requiring physical calibration.

### 3.3 CD-RCM Architecture

Inspired by the decoder-only transformer design of LVSM [Jin et al., 2025], we train a feedforward depth-queryable model that renders intermediate slices between acquired slices. Unlike LVSM, which operates on surface views with geometric parallax, CD-RCM models purely axial variation and depth-conditioned reflectance.

**Tokenizing Input Views.** For each input view  $\mathbf{I}_i$ , we compute pixel-wise Plücker ray embeddings [Plücker, 1865]  $\mathbf{P}_i \in \mathbb{R}^{H \times W \times 6}$  from the virtual camera parameters, and tokenize both into non-overlapping  $p \times p$  patches following ViT [Dosovitskiy et al., 2021] to obtain  $\mathbf{I}_{ij}$  and  $\mathbf{P}_{ij}$ , respectively. We channel-wise concatenate each pair, and map to  $d$ -dimensional input patch tokens  $\mathbf{x}_{ij}$  via a linear layer:

$$\{\mathbf{x}_{ij}\}_{j=1}^{HW/p^2} = \text{Linear}_{\text{input}}(\text{Concat}(\mathbf{I}_{ij}, \mathbf{P}_{ij})) \in \mathbb{R}^d. \quad (4)$$

Lastly, we flatten these to obtain a 1D input token sequence  $\mathbf{x}_K$  of length  $K = NHW/p^2$ .

**Tokenizing Target Views.** For each target depth  $t = 1, \dots, T$ , we similarly compute Plücker embeddings  $\mathbf{P}_t$ , patchify into  $p \times p$  patches to obtain  $\mathbf{P}_{tj}$ , and map these to  $d$ -dimensional target tokens  $\mathbf{y}_{tj}$  by a linear layer:

$$\{\mathbf{y}_{tj}\}_{j=1}^{HW/p^2} = \text{Linear}_{\text{target}}(\mathbf{P}_{tj}) \in \mathbb{R}^d. \quad (5)$$

We flatten these to form a 1D target token sequence  $\mathbf{y}_L$  of length  $L = THW/p^2$ .

**Transformer-based Decoder.** We concatenate  $[\mathbf{x}_K, \mathbf{y}_L]$  and process the sequence with a decoder-only transformer comprising 24 self-attention blocks (with QK-normalization [Henry et al., 2020]) and MLPs. Here, the term *decoder* refers to a GPT-style architecture [Radford et al., 2019] without causal masking, *i.e.*, attention is bidirectional across all tokens. After transformation, we retain only the updated target tokens and apply a linear layer followed by sigmoid activation to recover pixel intensities:

$$\hat{\mathbf{I}}_\ell = \text{Sigmoid}(\text{Linear}_{\text{out}}(\hat{\mathbf{y}}_\ell)) \in \mathbb{R}^{p^2} \quad (6)$$

Finally, we unpatchify (reshape) the intensity patches to recover the 2D synthesized target slices  $\hat{\mathbf{I}}_t$ .

### 3.4 Skin-Specific Perceptual Feature Extractor

Standard perceptual losses [Johnson et al., 2016, Zhang et al., 2018] emphasize natural-image semantics over the micro-textural patterns that dominate RCM imagery. To provide supervision sensitive to skin-specific structures (cellular morphology, speckle statistics, layer-dependent contrast), we train a domain-adapted perceptual backbone on a large auxiliary dataset of RCM mosaic crops.

We initialize a ViT [Dosovitskiy et al., 2021] from self-supervised DINOv3 [Siméoni et al., 2025] and adapt it to the skin domain via LoRA [Hu et al., 2022] applied to all attention projections:

$$\phi_s(\cdot) = \phi_{\text{DINOv3}}(\cdot; \theta_{\text{base}} + \Delta\theta_{\text{LoRA}}), \quad (7)$$

where only  $\Delta\theta_{\text{LoRA}}$  is optimized. A teacher network  $\phi_t$  is maintained via EMA *i.e.*,  $\theta_t \leftarrow m\theta_t + (1 - m)\theta_s$ , with momentum coefficient  $m$ . We follow the standard DINO multi-crop training paradigm [Siméoni et al., 2025], where we generate 2 global ( $224 \times 224$ ) and 8 local ( $96 \times 96$ ) crops per image. The teacher processes global crops, while the student processes all crops, promoting local-global consistency and robustness. For training, we use cross-entropy distillation between student and teacher distributions, computing losses from both CLS and mean-pooled patch tokens. Once trained,  $\phi_s$  is frozen and used as a skin-specific feature extractor.

### 3.5 Training Objective

We train CD-RCM using a weighted combination of complementary photometric and perceptual losses:

$$\mathcal{L} = \underbrace{\mathcal{L}_{\text{MSE}}(\hat{\mathbf{I}}_t, \mathbf{I}_t)}_{\text{photometric loss}} + \underbrace{\lambda \cdot \mathcal{L}_{\text{LPIPS}}(\hat{\mathbf{I}}_t, \mathbf{I}_t) + \gamma \cdot \mathcal{L}_{\text{SPF}}}_{\text{perceptual loss}}, \quad (8)$$

where  $\lambda$  and  $\gamma$  are scalar weights.  $\mathcal{L}_{\text{MSE}}$  computes pixel-wise mean squared error between  $\hat{\mathbf{I}}_t$  and  $\mathbf{I}_t$ , enforcing structural accuracy.  $\mathcal{L}_{\text{LPIPS}}$  [Zhang et al., 2018] captures higher-order perceptual structure. Following [Imtiaz et al., 2025], we use LPIPS over the VGG-based loss [Johnson et al., 2016] of prior works [Zhang et al., 2024, Jin et al., 2025]. Our *skin-specific perceptual feature* loss,

$$\mathcal{L}_{\text{SPF}} = \frac{1}{T} \|\phi_s(\hat{\mathbf{I}}_t) - \phi_s(\mathbf{I}_t)\|_1, \quad (9)$$

complements  $\mathcal{L}_{\text{LPIPS}}$  by enforcing consistency in a feature space adapted to dermatologic imagery, encouraging preservation of diagnostically relevant morphological details.

### 3.6 Training and Inference

During training, we sample sequences of  $M$  consecutive slices from each stack, use the first, middle, and last as conditioning inputs  $\mathbf{I}_i$ , and randomly select four intermediate slices as targets  $\mathbf{I}_t$ . This randomized sampling across varying depth separations prevents overfitting to fixed spacing and enables generalization to arbitrary depths. At inference, CD-RCM takes any three evenly spaced slices and predicts target views at arbitrary intermediate depths in a single feedforward pass — no per-stack optimization, iterative refinement, or perceptual feature computation is required. Effectively, this allows synthesis at continuous axial positions, which, in practice, corresponds to generating non-integer-index slices between discretely acquired sections.

## 4 Experiments

We describe our experimental setup (Section 4.1) and discuss the results obtained (Section 4.2). We also ablate key design choices in Section 4.3.

### 4.1 Experimental Setup

**Dataset.** We conduct our experiments using a dataset comprising 216 RCM stacks acquired *in vivo*. Each stack corresponds to a single skin site and contains between 50 and 65 en-face optical sections sampled along the axial ( $z$ ) direction. Imaging was performed on healthy skin of volunteers without any special preparation, with images obtained from the arm and trunk of healthy volunteers aged 20–50 years. It is important to note that each stack originates from a distinct skin site, and even when acquired from the same subject, RCM images do not exhibit visual similarity across sites due to strong spatial and structural variability. As a result, stacks can be treated as independent samples; while subject-level metadata is unavailable, our train/test split is performed at the stack level and is effectively disjoint.

Data were collected using a commercially available reflectance confocal microscope (VivaScope 1500, Caliber Imaging and Diagnostics, Rochester, NY), a system widely used in clinical imaging and dermatologic studies [Rajadhyaksha et al., 2017, Atak et al., 2023]. The microscope employs a stabilized imaging window that adheres to the region of interest, ensuring a fixed lateral field of view during stack acquisition.

Each slice is a single-channel intensity image of resolution  $1000 \times 1000$  pixels, corresponding to a lateral resolution of approximately  $0.5 \mu\text{m}$ . The optical sectioning thickness (axial resolution) of the imaging system is approximately  $3 \mu\text{m}$ , while consecutive slices are acquired at  $1.5 \mu\text{m}$  intervals. This results in axial oversampling relative to the optical sectioning limit, yet the stacks remain strongly anisotropic due to the disparity between lateral and axial resolution.

**Preprocessing.** We register each stack using SIFT-based [Lowe, 2004] affine alignment implemented in Fiji [Schindelin et al., 2012] to reduce motion-induced inter-slice misalignment. After registration, we extract  $960 \times 960$  center crops to remove boundary artifacts from the imaging window

Method	PSNR $\uparrow$	SSIM $\uparrow$	LPIPS $\downarrow$	$\mathcal{L}_{SPF}$ $\downarrow$
B-Spline Interpolation	22.02	0.471	0.375	0.161
Cubic Spline Interpolation	22.09	0.469	0.378	0.163
Gaussian Interpolation	<u>22.87</u>	<u>0.522</u>	0.477	0.164
<b>CD-RCM (Ours)</b>	<b>23.36</b>	<b>0.581</b>	<b>0.314</b>	<b>0.145</b>

Table 1: **Quantitative comparison of CD-RCM.** Compared with classical interpolation methods, CD-RCM achieves the best performance across all metrics, improving both photometric fidelity (PSNR, SSIM) and perceptual similarity (LPIPS,  $\mathcal{L}_{SPF}$ ).

and resize to  $512 \times 512$  via bilinear interpolation. The final five slices of each stack are excluded due to low signal content. We use a train-test split of approximately 70/30, yielding 156 training and 60 evaluation stacks.

**Implementation Details.** We train CD-RCM on four NVIDIA A6000 GPUs using a coarse-to-fine strategy [Zhang et al., 2024, Jin et al., 2025]. We first train CD-RCM from scratch for 20k steps at  $256 \times 256$  resolution (batch size 8 per GPU), followed by 10k finetuning steps at  $512 \times 512$  (batch size 4 per GPU). We set  $M = 9$  for all reported results. At inference,  $10\times$  densification of a full stack takes 0.8 seconds on a single A6000. Additional hyperparameters and architectural details are provided in the Appendix.

## 4.2 Results

We compare CD-RCM with three conventional interpolation techniques: B-spline, cubic spline, and Gaussian interpolation, and evaluate performance using photometric metrics (PSNR, SSIM) and perceptual metrics (LPIPS,  $\mathcal{L}_{SPF}$ ). Details of the interpolation methods and evaluation metrics are provided in the Appendix.

As shown in Table 1, CD-RCM consistently outperforms all interpolation methods across both photometric and perceptual metrics. While Gaussian interpolation achieves relatively strong PSNR and SSIM among the baselines, all interpolation approaches exhibit higher perceptual errors due to their inability to model depth-dependent anatomical structure. In contrast, CD-RCM produces more accurate and perceptually consistent reconstructions, achieving the best results across all metrics.

In Figure 3, we qualitatively compare CD-RCM with the interpolation baselines. As highlighted in the insets, conventional interpolation methods struggle to accurately reconstruct layered tissue structures and fine cellular features due to the lack of anatomical priors. In contrast, CD-RCM generates anatomically plausible intermediate slices that preserve the structural continuity of the anatomical morphology, closely matching the ground truth.

Clinicians generally prefer reconstructions that preserve high-frequency details, even with mild noise, over overly smoothed images that obscure diagnostically relevant structures. In our experiments, several interpolation baselines—particularly Gaussian interpolation—introduce noticeable blur. Although this smoothing can improve PSNR, which favors reduced variance, it degrades perceptual fidelity and obscures diagnostically relevant detail. CD-RCM avoids this tradeoff, producing reconstructions that are both photometrically accurate and perceptually sharp.

**Cross-sectional views of densified stacks** Figure 4 shows the cross-sectional and arbitrary-plane visualization of CD-RCM-densified stacks. Using CD-RCM, we densify RCM stacks so that axial sampling matches the actual sample dimensions, enabling isotropic 3D visualization. We show sagittal and coronal cross-sections (left) and arbitrary oblique cuts at specified azimuth, elevation, and offset angles (right) for two example stacks. Compared to the sparsely sampled input stacks, CD-RCM produces markedly smoother structural transitions along the  $z$ -axis, reducing the staircase artifacts visible in the original cross-sections and revealing continuous tissue morphology that may facilitate identification of clinically relevant landmarks.

## 4.3 Ablation Study

We ablate key design choices of CD-RCM, mainly the training objective and the design of our skin-specific perceptual loss  $\mathcal{L}_{SPF}$ . All models are trained at  $256 \times 256$  resolution for 20k steps.

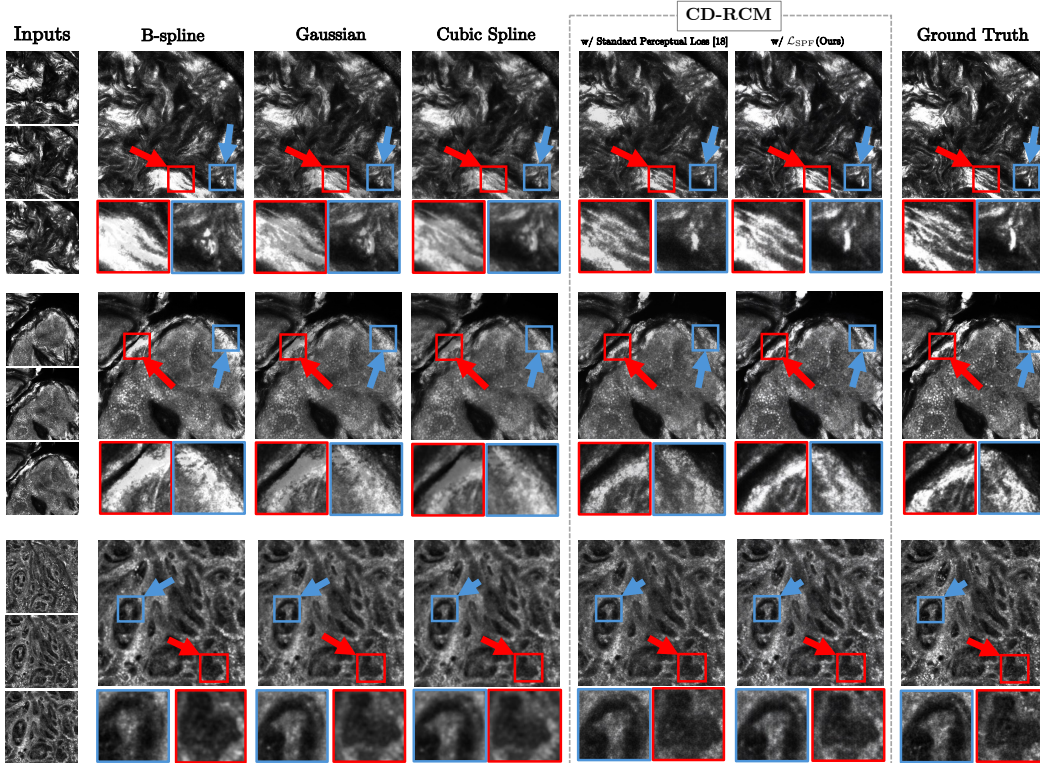


Figure 3: **Qualitative comparison of novel-depth synthesis methods.** We compare classical interpolation approaches with CD-RCM (with and without skin-specific perceptual supervision). CD-RCM best reconstructs fine cellular structures and depth-dependent texture transitions, producing results closest to the ground truth. Insets highlight regions where interpolation methods exhibit structural distortion and/or incorrect predictions.

Training objective	PSNR $\uparrow$	SSIM $\uparrow$	LPIPS $\downarrow$	$\mathcal{L}_{\text{SPF}} \downarrow$
$(\mathcal{L}_{\text{MSE}})$ + $\mathcal{L}_{\text{LPIPS}}$	21.60	0.480	0.343	0.273
+ Perceptual Loss [Johnson et al., 2016] + $\mathcal{L}_{\text{LPIPS}}$ + Perceptual Loss [Johnson et al., 2016]	22.56 <u>22.65</u>	0.547 <u>0.567</u>	0.386 <u>0.329</u>	0.258 <u>0.216</u>
+ $\mathcal{L}_{\text{LPIPS}}$ + $\mathcal{L}_{\text{SPF}}$ (multi-feature) + $\mathcal{L}_{\text{LPIPS}}$ + $\mathcal{L}_{\text{SPF}}$ (eq. (9))	22.39 <b>23.35</b>	0.522 <b>0.597</b>	0.338 <b>0.288</b>	0.246 <b>0.172</b>

Table 2: **Ablation of training objectives.** We compare different perceptual loss combinations for training CD-RCM. Best and second-best results are **bolded** and underlined, respectively. Our proposed  $\mathcal{L}_{\text{SPF}}$  (eq. (9)) yields the best performance across all metrics.

**Training Objective.** Table 2 reports performance across perceptual loss configurations, with  $\mathcal{L}_{\text{MSE}}$  included in all experiments. LPIPS alone yields the weakest results. The VGG-based perceptual loss of Johnson et al. [2016] performs better, and combining it with LPIPS further boosts performance. However, replacing the VGG-based loss with our proposed  $\mathcal{L}_{\text{SPF}}$  (eq. (9)) yields the best overall performance, simultaneously improving all four metrics. Figure 3 (columns 5 and 6) qualitatively confirms that  $\mathcal{L}_{\text{SPF}}$  produces higher-fidelity reconstructions that more closely match the ground truth.

**Design of  $\mathcal{L}_{\text{SPF}}$ .** We also ablate the design of  $\mathcal{L}_{\text{SPF}}$  by comparing our final-layer MAE formulation (eq. (9)) against a multi-layer feature variant analogous to the standard perceptual loss [Johnson et al., 2016]. As shown in the last two rows of Table 2, the single-layer design outperforms the multi-layer alternative across all metrics. CD-RCM demonstrates that feedforward novel-depth synthesis is a viable approach for densifying sparsely sampled RCM stacks, producing anatomically plausible intermediate slices in a single forward pass without per-stack optimization. This capability enables highly efficient stack densification, which may improve visualization and support downstream tasks.

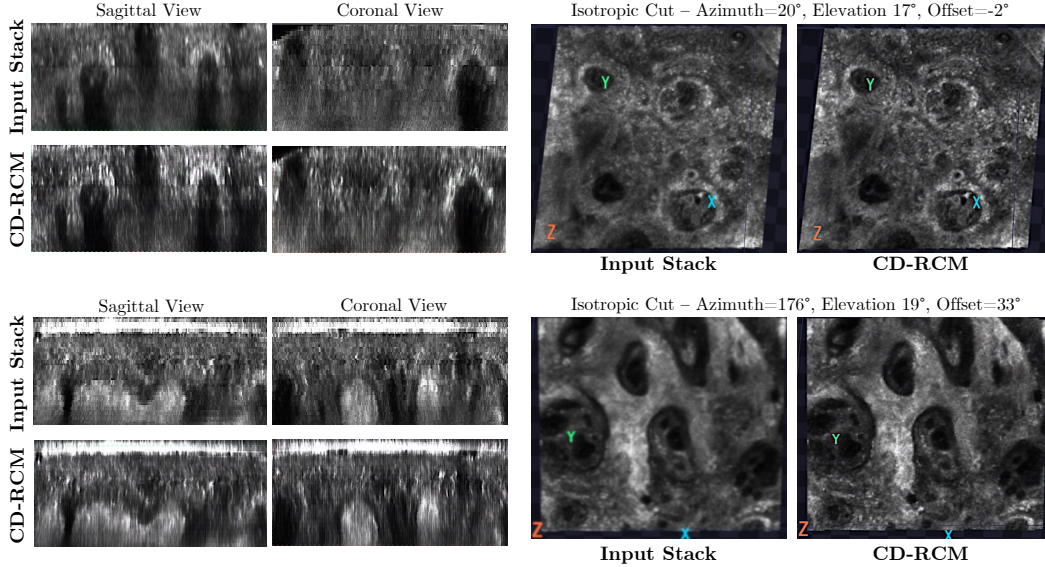


Figure 4: **Cross-sectional and arbitrary-plane visualization of densified stacks.** We densify the input stacks using CD-RCM to match the axial and lateral resolution of the actual sample, enabling isotropic 3D visualization. Sagittal, coronal, and oblique cross-sections show markedly smoother structural transitions compared to the sparsely sampled input stacks.

More broadly, our work illustrates how adapting modern neural rendering architectures to domain-specific imaging physics can open new possibilities for computational microscopy. A promising direction is to accelerate stack acquisition by sparsely sampling tissue sections and reconstructing intermediate slices with CD-RCM. This could speed up clinical imaging and reduce motion artifacts by shortening the time patients must remain still (see Limitations on registration).

#### 4.4 Limitations

Our pipeline uses SIFT-based registration to reduce inter-slice motion, but residual misalignment persists in some stacks and can degrade reconstruction quality. Moreover, curating a larger and more diverse dataset, spanning a wider range of skin types, and filtering out slices with low signal content may further improve robustness and performance.

#### 4.5 Future Work

This work represents a first-of-its-kind, proof-of-concept study for continuous-depth reconstruction from sparse RCM stacks. Our goal is to motivate further development toward clinical applications, including larger-scale data collection and comprehensive human studies.

Future work will integrate CD-RCM into interactive clinical visualization tools to evaluate whether densified stacks improve downstream analyses, such as DEJ localization and strata delineation. We also aim to extend CD-RCM to RCM mosaics acquired at consecutive depths to enable dense visualization over larger tissue regions. Finally, adapting our framework to other optical sectioning modalities, such as line-field confocal OCT (LC-OCT), could broaden its impact beyond RCM.

## 5 Conclusion

We introduced CD-RCM, the first feedforward framework for continuous-depth novel-view synthesis tailored to reflectance confocal microscopy. By modeling RCM acquisition as a virtual camera undergoing axial translation and leveraging a decoder-only transformer architecture, CD-RCM synthesizes anatomically plausible en face slices at arbitrary query depths from sparsely sampled stacks — without per-stack optimization and with sub-second inference time. We further proposed a skin-specific perceptual feature loss, trained via self-supervised domain adaptation on RCM mosaics, which provides supervisory signal attuned to the micro-textural patterns of confocal skin imaging. Our experiments demonstrate that CD-RCM outperforms conventional interpolation baselines across photometric and perceptual metrics, and ablations confirm the contribution of each design choice. By enabling post-hoc axial densification and arbitrary-orientation virtual sectioning, CD-RCM takes a step toward making continuous 3D visualization of in vivo skin a practical clinical tool.

## Acknowledgments

This work is partially supported by grants DoD/USAMRAA HT94252410553 and DoD/USAMRAA HT94252410554 and NIH/NCI R01CA199673.

## References

- Mehmet Fatih Atak, Banu Farabi, Cristian Navarrete-Dechent, Gennady Rubinstein, Milind Rajadhyaksha, and Manu Jain. Confocal microscopy for diagnosis and management of cutaneous malignancies: clinical impacts and innovation. *Diagnostics*, 13(5):854, 2023.
- A Bozkurt, K Kose, C Alessi-Fox, JG Dy, DH Brooks, and M Rajadhyaksha. Unsupervised delineation of stratum corneum using reflectance confocal microscopy and spectral clustering. *Skin Research and Technology*, 23(2):176–185, 2017.
- Alican Bozkurt, Kivanc Kose, Jaume Coll-Font, Christi Alessi-Fox, Dana H Brooks, Jennifer G Dy, and Milind Rajadhyaksha. Skin strata delineation in reflectance confocal microscopy images using recurrent convolutional networks with attention. *Scientific reports*, 11(1):12576, 2021.
- Yuanhao Cai, Yixun Liang, Jiahao Wang, Angtian Wang, Yulun Zhang, Xiaokang Yang, Zongwei Zhou, and Alan Yuille. Radiative gaussian splatting for efficient x-ray novel view synthesis. In *European Conference on Computer Vision*, pages 283–299. Springer, 2024.
- David Charatan, Sizhe Lester Li, Andrea Tagliasacchi, and Vincent Sitzmann. pixelsplat: 3d gaussian splats from image pairs for scalable generalizable 3d reconstruction. In *CVPR*, pages 19457–19467, 2024.
- Tianqi Chen, Bing Xu, Chiyuan Zhang, and Carlos Guestrin. Training deep nets with sublinear memory cost. *arXiv preprint arXiv:1604.06174*, 2016.
- Julian Chibane, Gerard Pons-Moll, et al. Neural unsigned distance fields for implicit function learning. *Advances in Neural Information Processing Systems*, 33:21638–21652, 2020.
- Tri Dao, Dan Fu, Stefano Ermon, Atri Rudra, and Christopher Ré. Flashattention: Fast and memory-efficient exact attention with io-awareness. volume 35, pages 16344–16359, 2022.
- Alexey Dosovitskiy, Lucas Beyer, Alexander Kolesnikov, Dirk Weissenborn, Xiaohua Zhai, Thomas Unterthiner, Mostafa Dehghani, Matthias Minderer, Georg Heigold, Sylvain Gelly, Jakob Uszkoreit, and Neil Houlsby. An image is worth 16x16 words: Transformers for image recognition at scale. In *ICLR*, 2021.
- SJ Edwards, G Osei-Assibey, R Patalay, V Wakefield, and C Karner. Diagnostic accuracy of reflectance confocal microscopy using vivascope for detecting and monitoring skin lesions: a systematic review. *Clinical and Experimental Dermatology*, 42(3):266–275, 2017.
- Esmail Enjilela, Ting-Yim Lee, Gerald Wisenberg, Patrick Teefy, Rodrigo Bagur, Ali Islam, Jiang Hsieh, and Aaron So. Cubic-spline interpolation for sparse-view ct image reconstruction with filtered backprojection in dynamic myocardial perfusion imaging. *Tomography*, 5(3):300, 2019.
- Sindhu Ghanta, Michael I Jordan, Kivanc Kose, Dana H Brooks, Milind Rajadhyaksha, and Jennifer G Dy. A marked poisson process driven latent shape model for 3d segmentation of reflectance confocal microscopy image stacks of human skin. *IEEE Transactions on Image Processing*, 26(1): 172–184, 2016.
- Salvador Gonzalez, M. Gill, and Allan C. Halpern, editors. *Reflectance Confocal Microscopy of Cutaneous Tumors: An Atlas with Clinical, Dermoscopic and Histological Correlations*. CRC Press, 1 edition, 2008. doi: 10.3109/9780203091562.
- Alex Henry, Prudhvi Raj Dachapally, Shubham Shantaram Pawar, and Yuxuan Chen. Query-key normalization for transformers. In *Findings of the Association for Computational Linguistics: EMNLP 2020*, pages 4246–4253, 2020.

- Yicong Hong, Kai Zhang, Jiuxiang Gu, Sai Bi, Yang Zhou, Difan Liu, Feng Liu, Kalyan Sunkavalli, Trung Bui, and Hao Tan. Lrm: Large reconstruction model for single image to 3d. *ICLR*, 2024.
- Edward J Hu, Yelong Shen, Phillip Wallis, Zeyuan Allen-Zhu, Yuanzhi Li, Shean Wang, Liang Wang, Weizhu Chen, et al. Lora: Low-rank adaptation of large language models. *Iclr*, 1(2):3, 2022.
- Misbah Huzaira, Francisca Rius, Milind Rajadhyaksha, R. Rox Anderson, and Salvador González. Topographic variations in normal skin, as viewed by in vivo reflectance confocal microscopy. *Journal of Investigative Dermatology*, 116(6):846–852, 2001. ISSN 0022-202X. doi: <https://doi.org/10.1046/j.0022-202x.2001.01337.x>. URL <https://www.sciencedirect.com/science/article/pii/S0022202X15412552>.
- Tooba Imtiaz, Lucy Chai, Kathryn Heal, Xuan Luo, Jungyeon Park, Jennifer Dy, and John Flynn. Lvt: Large-scale scene reconstruction via local view transformers. In *Proceedings of the SIGGRAPH Asia 2025 Conference Papers*, pages 1–12, 2025.
- Haian Jin, Hanwen Jiang, Hao Tan, Kai Zhang, Sai Bi, Tianyuan Zhang, Fujun Luan, Noah Snavely, and Zexiang Xu. Lvsm: A large view synthesis model with minimal 3d inductive bias. In *ICLR*, 2025.
- Justin Johnson, Alexandre Alahi, and Li Fei-Fei. Perceptual losses for real-time style transfer and super-resolution. In *European conference on computer vision*, pages 694–711. Springer, 2016.
- Bernhard Kerbl, Georgios Kopanas, Thomas Leimkühler, and George Drettakis. 3d gaussian splatting for real-time radiance field rendering. *ACM TOG*, 42(4):139–1, 2023.
- Kivanc Kose, Alican Bozkurt, Christi A Fox, Melissa Gill, Dana Brooks, Jennifer Dy, and Milind Rajadhyaksha. Detection of the dej and segmentation of its morphological patterns in rcm images of melanocytic skin lesions. In *Microscopy Histopathology and Analytics*, pages MW2A–1. Optica Publishing Group, 2020.
- Flora Latriglia, Jonas Ogien, Clara Tavernier, Sébastien Fischman, Mariano Suppa, Jean-Luc Perrot, and Arnaud Dubois. Line-field confocal optical coherence tomography (lc-oct) for skin imaging in dermatology. *Life*, 13(12), 2023. ISSN 2075-1729. doi: 10.3390/life13122268. URL <https://www.mdpi.com/2075-1729/13/12/2268>.
- Thomas Martin Lehmann, Claudia Gonner, and Klaus Spitzer. Survey: Interpolation methods in medical image processing. *IEEE transactions on medical imaging*, 18(11):1049–1075, 2002.
- Yingtai Li, Xueming Fu, Han Li, Shang Zhao, Ruiyang Jin, and S Kevin Zhou. 3dgr-ct: Sparse-view ct reconstruction with a 3d gaussian representation. *Medical Image Analysis*, 103:103585, 2025.
- Jonathan T.C. Liu, Adam K. Glaser, Chetan Poudel, and Joshua C. Vaughan. Nondestructive 3d pathology with light-sheet fluorescence microscopy for translational research and clinical assays. *Annual Review of Analytical Chemistry*, 16(Volume 16, 2023):231–252, 2023. ISSN 1936-1335. doi: <https://doi.org/10.1146/annurev-anchem-091222-092734>. URL <https://www.annualreviews.org/content/journals/10.1146/annurev-anchem-091222-092734>.
- Ilya Loshchilov and Frank Hutter. Decoupled weight decay regularization. *arXiv preprint arXiv:1711.05101*, 2017.
- David G Lowe. Distinctive image features from scale-invariant keypoints. *International journal of computer vision*, 60(2):91–110, 2004.
- Lars Mescheder, Michael Oechsle, Michael Niemeyer, Sebastian Nowozin, and Andreas Geiger. Occupancy networks: Learning 3d reconstruction in function space. In *Proceedings of the IEEE/CVF conference on computer vision and pattern recognition*, pages 4460–4470, 2019.
- Ben Mildenhall, Pratul P Srinivasan, Matthew Tancik, Jonathan T Barron, Ravi Ramamoorthi, and Ren Ng. Nerf: Representing scenes as neural radiance fields for view synthesis. In *ECCV*, 2020.
- Julius Plücker. Xvii. on a new geometry of space. *Philosophical Transactions of the Royal Society of London*, (155):725–791, 1865.

- Alec Radford, Jeffrey Wu, Rewon Child, David Luan, Dario Amodei, Ilya Sutskever, et al. Language models are unsupervised multitask learners. *OpenAI blog*, 1(8):9, 2019.
- Milind Rajadhyaksha, Ashfaq Marghoob, Anthony Rossi, Allan C. Halpern, and Kishwer S. Nehal. Reflectance confocal microscopy of skin in vivo: From bench to bedside. *Lasers in Surgery and Medicine*, 49(1):7–19, 2017. doi: <https://doi.org/10.1002/lsm.22600>. URL <https://onlinelibrary.wiley.com/doi/abs/10.1002/lsm.22600>.
- N. A. Richarz, A. Boada, A. Jaka, J. Bassas, C. Ferrándiz, J. M. Carrascosa, and O. Yélamos. Challenges for new adopters in pre-surgical margin assessment by handheld reflectance confocal microscope of basal cell carcinoma: A prospective single-center study. *Dermatology Practical & Conceptual*, 12(4):e2022162, Oct 2022. doi: 10.5826/dpc.1204a162.
- Johannes Schindelin, Ignacio Arganda-Carreras, Erwin Frise, Verena Kaynig, Mark Longair, Tobias Pietzsch, Stephan Preibisch, Curtis Rueden, Stephan Saalfeld, Benjamin Schmid, et al. Fiji: an open-source platform for biological-image analysis. *Nature methods*, 9(7):676–682, 2012.
- Oriane Siméoni, Huy V Vo, Maximilian Seitzer, Federico Baldassarre, Maxime Oquab, Cijo Jose, Vasil Khalidov, Marc Szafraniec, Seungeun Yi, Michaël Ramamonjisoa, et al. Dinov3. *arXiv preprint arXiv:2508.10104*, 2025.
- Andrew H. Song, Mane Williams, Drew F.K. Williamson, Sarah S.L. Chow, Guillaume Jaume, Gan Gao, Andrew Zhang, Bowen Chen, Alexander S. Baras, Robert Serafin, Richard Colling, Michelle R. Downes, Xavier Farré, Peter Humphrey, Clare Verrill, Lawrence D. True, Anil V. Parwani, Jonathan T.C. Liu, and Faisal Mahmood. Analysis of 3d pathology samples using weakly supervised ai. *Cell*, 187(10):2502–2520.e17, 2024. ISSN 0092-8674. doi: <https://doi.org/10.1016/j.cell.2024.03.035>. URL <https://www.sciencedirect.com/science/article/pii/S0092867424003519>.
- Monika Wojarska, Klaudia Kokot, Paulina Bernecka, Natalia Domańska, Agata Libik, Dana Bunevich, Dominika Nowakowska, Magdalena Dzido, Wiktoria Borzyszkowska, Wojciech Kazimierczak, and Jerzy Jankau. In vivo confocal microscopy in the surgical treatment of keratinocyte carcinomas: A systematic review. *Journal of Clinical Medicine*, 14(16), 2025. ISSN 2077-0383. doi: 10.3390/jcm14165779. URL <https://www.mdpi.com/2077-0383/14/16/5779>.
- Ruyi Zha, Tao Jun Lin, Yuanhao Cai, Jiwen Cao, Yanhao Zhang, and Hongdong Li. R<sup>2</sup>-gaussian: Rectifying radiative gaussian splatting for tomographic reconstruction. In *Advances in Neural Information Processing Systems (NeurIPS)*, 2024.
- Kai Zhang, Sai Bi, Hao Tan, Yuanbo Xiangli, Nanxuan Zhao, Kalyan Sunkavalli, and Zexiang Xu. Gs-irm: Large reconstruction model for 3d gaussian splatting. In *ECCV*, pages 1–19. Springer, 2024.
- Richard Zhang, Phillip Isola, Alexei A Efros, Eli Shechtman, and Oliver Wang. The unreasonable effectiveness of deep features as a perceptual metric. In *CVPR*, pages 586–595, 2018.

## A Further Implementation Details

### A.1 Skin-specific perceptual feature extractor

For training the skin-specific perceptual feature extractor  $\phi_s$  (Sec. 3.5), we use LoRA with rank 16 and optimize using AdamW Loshchilov and Hutter [2017] with a constant learning rate of  $1 \times 10^{-4}$ . The teacher network is updated using EMA with momentum  $m = 0.9995$ . The projection MLP  $h$  has a bottleneck dimension of 256 and an output dimension of 4096. The teacher and student temperatures in Eqs. 9 and 10 are set to  $\tau_t = 0.04$  and  $\tau_s = 0.1$ , respectively. We train the model for 4 epochs using one NVIDIA A6000 GPU, which takes 3 days.

## A.2 CD-RCM

For training CD-RCM (Sec. 3.6), we tokenize images and Plücker embeddings using a patch size  $p = 8$ , and set the embedding dimension (Eqs. 6 and 7)  $d = 768$  of the linear projectors. For optimization, we use AdamW Loshchilov and Hutter [2017] with  $\beta_1 = 0.9$ ,  $\beta_2 = 0.95$ , and a weight decay of 0.05 applied to all parameters except LayerNorm layers. We employ a cosine learning rate schedule with linear warmup, using 2000 warmup steps and a peak learning rate of  $4 \times 10^{-4}$  for both training resolutions. The loss weights in Eq. 12 are set to  $\lambda = 0.5$  and  $\gamma = 0.05$ . The full model has 170.8M trainable parameters. We train CD-RCM using four NVIDIA A6000 GPUs. The first stage of training (*i.e.*, at 256 resolution) takes 2 days, and finetuning at 512 resolution takes another 2 days.

Following Jin et al. [2025], we use gradient skipping for gradient norm  $> 5.0$  and gradient-clipping at 1.0 to stabilize training. Lastly, to boost training and inference efficiency, we use FlashAttention-v2 Dao et al. [2022] within the attention blocks, gradient checkpointing Chen et al. [2016], and mixed-precision training with BF16 data type.

## B Baselines Methods

We adopt three well-established classical interpolation techniques widely adopted for processing medical imaging data as the baselines in our experiments Enjilela et al. [2019], Lehmann et al. [2002].

Note that simply training a neural network to predict intermediate frames would, at best, only allow interpolating at fixed, predetermined intermediate depths, unlike the capability of CD-RCM to generalize to predict *any* intermediate depth. We additionally evaluated a diffusion-based model for intermediate slice prediction, but it failed to reconstruct high-frequency structures. This is consistent with the known data requirements of diffusion models and their sensitivity to noisy inputs, which are characteristic of RCM imagery.

Below, we explain each interpolation technique:

### B.1 B-Spline Interpolation.

B-spline interpolation models the intensity along the axial direction as a smooth spline function and evaluates it at intermediate depths. For our case, it treats the three input slices as samples of a smooth intensity function along the axial direction and estimates missing slices by applying third-order spline interpolation independently at each pixel location. For each pixel location  $(x, y)$ , let the observed slices be  $I(z_i, x, y)$  for  $i \in \{1, \dots, N\}$ . The interpolated intensity at depth  $z$  is computed as

$$\hat{I}(z, x, y) = \sum_k c_k(x, y) \beta_3(z - k), \quad (10)$$

where  $\beta_3(\cdot)$  denotes the cubic B-spline basis function and  $c_k(x, y)$  are spline coefficients derived from the observed samples. In practice, we implement this interpolation using `map_coordinates` of `scipy.ndimage` library with spline order 3, which evaluates the cubic B-spline along the depth axis independently for each pixel.

### B.2 Cubic Spline Interpolation.

Cubic spline interpolation fits a natural cubic spline along the depth axis for each pixel independently, using the three observed slices as control points. Given observed samples  $(z_i, I(z_i, x, y))$ , a piecewise cubic polynomial is constructed, such that

$$S(z) = \begin{cases} a_1 z^3 + b_1 z^2 + c_1 z + d_1, & z_1 \leq z < z_2 \\ \vdots & \\ a_{N-1} z^3 + b_{N-1} z^2 + c_{N-1} z + d_{N-1}, & z_{N-1} \leq z \leq z_N \end{cases} \quad (11)$$

such that

$$S(z_i) = I(z_i, x, y), \quad S'(z_i^-) = S'(z_i^+), \quad S''(z_i^-) = S''(z_i^+), \quad (12)$$

with natural boundary conditions

$$S''(z_1) = S''(z_N) = 0. \quad (13)$$

Intermediate slices are obtained by evaluating  $S(z)$  at the desired depths  $z$ .

We implement this method using CubicSpline function of `scipy.interpolate` with boundary condition set to `natural`, *i.e.*, the second derivative at curve ends are zero (eq. (13)).

### B.3 Gaussian Interpolation.

Gaussian interpolation first generates intermediate slices using cubic B-spline interpolation and then applies spatial Gaussian smoothing to each synthesized slice. Let  $\tilde{I}(z, x, y)$  denote the B-spline interpolated slice. The final result is obtained by convolving each slice with a Gaussian kernel:

$$\hat{I}(z, x, y) = (\tilde{I} * G_\sigma)(x, y) = \sum_{u,v} \tilde{I}(z, x - u, y - v) G_\sigma(u, v), \quad (14)$$

where

$$G_\sigma(u, v) = \frac{1}{2\pi\sigma^2} \exp\left(-\frac{u^2 + v^2}{2\sigma^2}\right). \quad (15)$$

We use  $\sigma = 1$  in our implementation. This smoothing produces visually smooth transitions across depths but suppresses high-frequency cellular structures.

## C Evaluation Metrics

We evaluate reconstruction quality using both photometric and perceptual metrics. Specifically, we report peak signal-to-noise ratio (PSNR), structural similarity (SSIM), and the learned perceptual image patch similarity (LPIPS). We also use our proposed skin-specific perceptual feature loss  $\mathcal{L}_{\text{SPF}}$  (Eq. 13) as a skin domain-aware perceptual similarity metric.

### C.1 PSNR

Peak signal-to-noise ratio (PSNR) measures pixel-wise reconstruction fidelity between a predicted image  $\hat{I}$  and the ground truth image  $I$ . It is defined as:

$$\text{PSNR} = 10 \log_{10} \left( \frac{\text{MAX}^2}{\text{MSE}} \right), \quad (16)$$

where MAX denotes the maximum possible pixel intensity (*i.e.*, 255 in our case), and MSE is the mean squared error:

$$\text{MSE} = \frac{1}{HW} \sum_{x,y} (I(x, y) - \hat{I}(x, y))^2. \quad (17)$$

Higher PSNR values indicate better reconstruction fidelity.

## C.2 SSIM

Structural Similarity Index (SSIM) evaluates perceptual image quality by comparing luminance, contrast, and structural information between two images. It is defined as:

$$\text{SSIM}(I, \hat{I}) = \frac{(2\mu_I\mu_{\hat{I}} + C_1)(2\sigma_{I\hat{I}} + C_2)}{(\mu_I^2 + \mu_{\hat{I}}^2 + C_1)(\sigma_I^2 + \sigma_{\hat{I}}^2 + C_2)}, \quad (18)$$

where  $\mu$ ,  $\sigma^2$ , and  $\sigma_{I\hat{I}}$  denote the mean, variance, and covariance of the images, respectively, and  $C_1$ ,  $C_2$  are constants used for numerical stability. SSIM ranges from  $-1$  to  $1$ , with higher values indicating greater structural similarity.

## C.3 LPIPS

Learned Perceptual Image Patch Similarity (LPIPS) Zhang et al. [2018] measures perceptual similarity in the feature space of a pretrained convolutional network (we use the VGG backbone in our implementation, as it is shown in the original paper to be the strongest variant). Given feature activations  $\phi_l(\cdot)$  at layer  $l$ , LPIPS is computed as

$$\text{LPIPS}(I, \hat{I}) = \sum_l w_l \|\phi_l(I) - \phi_l(\hat{I})\|_2^2, \quad (19)$$

where  $w_l$  are learned channel-wise weights. Unlike pixel-based metrics, LPIPS better captures perceptual differences in texture and structure. Lower LPIPS values indicate greater perceptual similarity.

## D Additional Qualitative Results

### D.1 Videos of densified stacks

To complement the cross-sections visualized above, we also include videos of the en face views of the densified stacks using CD-RCM and the evaluation baselines. Classical interpolation methods produce visually smooth transitions between the sparse input slices. However, these novel depth views carry little plausibility as they are not based on any anatomical priors, but only utilize the pixel values across the sparse inputs to hallucinate the intermediate representations. On the contrary, CD-RCM produces smoothly transitioning, anatomically plausible intermediate depth slices.

## E Broader Impacts

This work has potential positive societal impact in biomedical imaging and clinical workflows. By enabling continuous-depth reconstruction from sparse RCM stacks, CD-RCM may improve visualization, reduce acquisition burden, and support more consistent analysis of skin microstructure. In the long term, such tools could assist clinicians in diagnosis and monitoring, particularly in settings where dense sampling is time-consuming or impractical.

Potential negative impacts may arise from over-reliance on synthesized data. As CD-RCM generates intermediate slices that are not directly observed, there is a risk that inaccuracies or hallucinated structures could be misinterpreted as real tissue features, potentially affecting clinical decisions if used without appropriate validation. To mitigate these risks, CD-RCM should be used with clear communication that synthesized slices are model predictions.

Additionally, the current model is a proof-of-concept study and is trained on a limited dataset of healthy skin from a single imaging setup. To broaden generalization across populations, devices, or pathological conditions, more exhaustive, diverse data should be collected for training and evaluating the model, incorporating uncertainty estimation, and validating the method in downstream clinical tasks before deployment in real-world settings. The same is discussed in Section 4.5.